








RESEARCH ARTICLE | MARCH 25 2026

An advanced immersed fluid–structure interaction particle method for cardiovascular applications experimentally validated vs a new benchmark case

Alessandra Monteleone ; Sofia Di Leonardo ; Marco Correnti ; Enrico Napoli ; Giorgio Micale ; Gaetano Burriesci  



Physics of Fluids 38, 031913 (2026)

<https://doi.org/10.1063/5.0315544>



Articles You May Be Interested In

Graphics processing unit accelerated modeling of thrombus formation in cardiovascular systems using smoothed particle hydrodynamics

Physics of Fluids (February 2025)

Hemodynamics of slip surfaces for thrombosis control in implanted cardiovascular devices

Physics of Fluids (February 2025)

A revised and expanded unified theory linking wall shear stress and vorticity topologies to enable the interpretation of cardiovascular flow disturbances

Physics of Fluids (March 2025)

AIP Advances

Why Publish With Us?



21DAYS
average time
to 1st decision



OVER 4 MILLION
views in the last year



INCLUSIVE
scope

Learn More



An advanced immersed fluid–structure interaction particle method for cardiovascular applications experimentally validated vs a new benchmark case



Cite as: Phys. Fluids **38**, 031913 (2026); doi: 10.1063/5.0315544

Submitted: 7 December 2025 · Accepted: 3 March 2026 ·

Published Online: 25 March 2026



View Online



Export Citation



CrossMark

Alessandra Monteleone,¹ Sofia Di Leonardo,¹ Marco Correnti,^{1,2} Enrico Napoli,² Giorgio Micale,² and Gaetano Burriesci^{1,2,3,a)}

AFFILIATIONS

¹Group of Bioengineering & Medical Devices, Ri.MED Foundation, Via Bandiera 11, 90133 Palermo, Italy

²Department of Engineering, University of Palermo, Viale delle Scienze, 90128 Palermo, Italy

³UCL Mechanical Engineering, University College London, Torrington Place, London WC1E 7JE, United Kingdom

^{a)}Author to whom correspondence should be addressed: gaetano.burriesci@unipa.it. Tel.: +39 091 2389 7251

ABSTRACT

Fluid–structure interaction (FSI) is crucial in the numerical simulation of cardiovascular phenomena, where pulsatile blood flow dynamically interacts with highly deformable tissues. High-fidelity FSI approaches have become essential to enhance the understanding of potentially lethal pathologies, assisting diagnosis and development of novel therapeutic solutions. This work presents and experimentally validates a new, totally meshless FSI approach, specifically designed for cardiovascular applications. The method is based on the Lagrangian smoothed particle hydrodynamics (SPH), employing a unified physics to represent both blood and deformable walls, avoiding FSI interfaces. A key advantage of this method lies in its ability to overcome the SPH complex issue in contour management, a common challenge that typically increases the complexity of this methodology in FSI applications. Deformable walls are immersed in the fluid domain, and a buffer region of fluid is defined to handle the structural deformation. For validation, a new FSI benchmark is proposed and analyzed with the particle image velocimetry technique. Tailored to entail the typical complexities of relevant cardiovascular situations, the benchmark involves pulsatile flow interacting with a chamber with deformable curved walls, moving through both filling and emptying phases. Despite its simplified geometry, designed to allow a reliable experimental validation, the structure experiences a field of three-dimensional strains and large volume variations, thereby replicating complexities often associated with more intricate models. Numerical and experimental results show good agreement in terms of fluid velocity field and structural deformation, establishing the proposed totally meshless FSI approach as a reliable tool for complex cardiovascular modeling.

© 2026 Author(s). All article content, except where otherwise noted, is licensed under a Creative Commons Attribution (CC BY) license (<https://creativecommons.org/licenses/by/4.0/>). <https://doi.org/10.1063/5.0315544>

I. INTRODUCTION

Fluid–structure interaction (FSI) is a pivotal and ubiquitous mechanism in various technological fields, particularly in cardiovascular bioengineering.^{1–3} In the cardiocirculatory system, pulsatile blood flows dynamically interact with highly deformable tissues, such as vessel walls, heart chambers, and valves. Recognizing that cardiovascular diseases are the leading cause of global morbidity and mortality,⁴ accurate simulation of cardiovascular FSIs has become a priority in biomechanics.^{1,5} In this scenario, thanks to the increase in computational power

and availability of resources,⁶ numerical FSI methods are becoming fundamental tools aimed at improving the understanding of physiological phenomena,⁷ assisting the diagnosis of cardiovascular pathologies,^{8,9} as well as lead the development and optimization of medical devices and treatments.^{10,11} Numerical FSI methods have been widely used to investigate the hemodynamics of native (healthy and pathological)^{7,12–14} and artificial heart valves,^{15–20} coronary arteries,^{21,22} the progression of conditions like atherosclerosis,^{23–25} aortic dissections,²⁶ abdominal aortic aneurysm,^{27–29} and cerebral aneurysm.^{30–33}

Furthermore, FSI approaches have been employed for assessing the blood stasis and the associated potential thromboembolic risk in the left atrial appendage (LAA).^{8,34}

In FSI simulations, computational fluid and structural dynamics (CFD and CSD, respectively) are coupled using partitioned or monolithic approaches.^{35–37} In the former, fluid and structural computational domains are solved separately and the solutions are then matched using one-way (weak coupling, only fluid influences structural results, or *vice versa*) or two-way schemes (strong coupling, fluid and structure affect each other).³⁸ On the other hand, in monolithic FSI, a single system of equations is used to solve simultaneously fluid and structural domains.³⁹

Conventional FSI approaches typically employ grid-based methods, coupling an Eulerian formulation for the fluid domain based on the finite volume method (FVM) with a Lagrangian formulation for the structural domain, generally based on the finite element method (FEM). The interaction between the two computational domains is handled with suitable algorithms, among which the most used in cardiovascular FSI simulations are the arbitrary Lagrangian Eulerian (ALE)^{40–42} and the immersed boundary (IB).^{43–46} The ALE approach, implemented both in partitioned or monolithic FSI schemes, employs a boundary fitted mesh that moves with a smoothed and arbitrary velocity.^{1,47} The main drawback of ALE is the need for a continuous update of the mesh and boundary conditions, which leads to heavy computational efforts.^{48,49} The IB method, first introduced by Peskin⁵⁰ to simulate the hemodynamics of heart valves, avoids the mesh regeneration issue of ALE and is therefore more efficient in applications characterized by large deformations.⁴⁵ The method, typically implemented in partitioned FSI schemes, uses a fixed mesh for the fluid domain and a deformable mesh for the structure. Overlapping regions between fluid and structural domains are identified, and a force term is added in the fluid equations to deal with the presence of the structure. Both ALE and IB coupling techniques encounter difficulties in the modeling of phenomena where the domain separates into unconnected regions, such as that occurring with the closing of heart or vascular valves.^{51–53}

Alternative FSI strategies are based on meshless numerical methods.⁵⁴ Among these, smoothed particle hydrodynamics (SPH) stands out.^{55–58} This Lagrangian particle-based method was first proposed by Lucy⁵⁹ and by Gingold and Monahan⁶⁰ to simulate interstellar flows, and afterward applied in various fields of engineering and science.^{61,62} In FSI modeling, SPH has been combined with FEM^{63–65} or other approaches such as the element bending group method,^{66,67} the smoothed point interpolation method,⁶⁸ or particle–spring systems.⁶⁹ Other FSI approaches have been proposed, where SPH is employed to describe both fluid and solid domains, using the weakly compressible (WCSPH)^{55,70} and the truly incompressible (ISPH)^{71,72} techniques. In 2024, Monteleone *et al.*⁷³ proposed a mono-physics FSI approach fully integrated in the ISPH scheme, where a single algorithm and physics are employed to solve fluid and structural domains. The mono-physics FSI method is especially suited for cardiovascular problems, where structures typically consist of biological soft tissues, and exhibit incompressibility and similar density to blood.^{51,74–77} Moreover, it offers significant advantages over traditional FSI strategies for biological valve modeling, enabling complete valve coaptation with no need for remeshing or complex interface management. This method was successfully applied to model the dynamics of the aortic valve leaflets,

describing the aortic wall as a rigid boundary.⁷³ In the context of thrombus formation modeling, the same research group⁷⁸ also implemented a similar FSI approach, where the structural domain is not pre-defined (as in Ref. 73) but it is dynamically generated to model the formation and growth of blood clots. This approach was recently used in Lo Presti *et al.*⁷⁹ to model thrombus formation, growth, and embolization within the LAA, imposing a prescribed motion on the chamber walls to model atrial fibrillation dynamics. This necessarily neglects the dynamic changes in the wall velocity caused by the thrombus presence as this forms, thus overlooking the direct interaction between the LAA tissue and the blood flow.

In the present work, the mono-physics FSI approach⁷³ is extended to the modeling of deformable walls. Both fluid and structural domains are represented with SPH particles, with spring links added between the particles belonging to the solid domain to describe the structural response. The solid domain is immersed in the fluid domain, which includes a buffer volume larger than the region expected to be enveloped by the structure during its motion. Three types of particles are thus defined, depending on the region to which they belong: *effective fluid* particles (inside the fluid domain), *solid* particles (in the structural domain), and *reservoir fluid* particles (in the buffer region). The latter are free to enter in/leave the computational domain through open boundaries, employing the procedure described in Monteleone *et al.*⁸⁰ Each particle interacts with its neighboring particle, independently of their type, following the ISPH formulation. This FSI approach is fully meshless, as it does not require the definition of FSI interfaces, whose handling represents a very challenging task for computational methods.²

This method is here validated vs a new benchmark test specifically designed to simulate relevant challenges in cardiovascular problems. Specifically, a structure made from a highly deformable incompressible material is subjected to a pulsatile fluid flow, while ensuring straightforward experimental replication and analysis. The structure geometry can be regarded as an idealization of common anatomical structures such as the LAA or an aneurysm, allowing for relevant, although simplified, FSI studies in complex cardiovascular settings. Experimental tests are analyzed using particle image velocimetry (PIV), which is a gold standard in experimental flow characterization^{1,81,82} and is widely used for the validation of numerical simulations.^{7,83–85} Reference data of the recommended benchmark (geometry and boundary conditions), alongside numerical and experimental results (in terms of flow velocity and structural deformation), are provided to support validation of other computational FSI methods in this field.

II. METHODS

A. Numerical method

A mono-physics FSI approach⁷³ is adopted in this study, integrated into the PANORMUS (PARallel Numerical Open-souRce Model for Unsteady flow Simulations) software.⁸⁶ A concise overview of the methodology is provided below, specifically highlighting its novel application, as presented in the current work, for modeling the interaction between deformable walls and pulsatile flows. The governing equations and numerical formulation are described only to the extent necessary to understand the FSI treatment, particle-based structural modeling, and experimental validation aspects. For the

comprehensive mathematical details and derivation of the ISPH scheme, the reader is referred to Ref. 73.

Based on the meshless SPH, the approach represents both fluid and solid computational domains with a set of particles. Adhering to the Lagrangian formulation, the particles move transporting their properties. The field variables at each particle are calculated through discrete convolution integrals with filter functions, named *kernel functions* (W), that are characterized by a specific length h (noted as *smoothing length*) and constant k . The length controls the influence domain of each i particle, including all the neighboring particles j having a distance from i less than kh . Therefore, a generic function φ at particle i located at position \mathbf{x}_i can be obtained by interpolating the values of the neighboring particles j ,

$$\varphi_i = \sum_{j=1}^{N_i} \frac{m_j}{\rho_j} \varphi_j W_{ij}, \quad (1)$$

where N_i is the total number of j particles neighbor to i ; m_j and ρ_j represent mass and density of j ; and $W_{ij} = W(\mathbf{x}_i - \mathbf{x}_j, h)$.

Governing equations, consisting of momentum and continuity equations for incompressible fluids, are solved employing an incompressible SPH (ISPH) algorithm. The numerical scheme, which follows the fractional-step technique of Chorin,⁸⁷ is based on predictor-corrector steps as detailed in Monteleone *et al.*^{80,88} In the predictor-step, the momentum equation is first solved, neglecting the pressure gradient term, to obtain an intermediate non-solenoidal velocity. Following this, in the corrector-step, a pressure correction is applied to enforce incompressibility, adjusting the predicted velocities to ensure mass conservation. The pressure field is determined implicitly by solving a system of pressure Poisson equations using the BiConjugate Gradient Stabilized method.⁸⁹

The mirror particle procedure⁸⁶ is used at solid fixed walls to impose suitable boundary conditions and to overcome the truncation of the *kernel function*, while the technique proposed by Monteleone *et al.*⁸⁰ is used at the open boundaries.

Furthermore, the shifting procedure proposed by Xu *et al.*⁹⁰ is used to maintain a more uniform particle distribution during

computation, reducing the well-known *tensile instability* issue,^{91–93} which leads to particle clustering/blowing away. This procedure consists of shifting slightly the particles across streamlines, allowing an ordered particle distribution to be maintained over time. The values of the hydrodynamic variables are thus adjusted at the new position through a Taylor series expansion. It should be noted that the procedure of Xu *et al.*⁹⁰ is applied only to fluid particles, without introducing further stabilization algorithms for the structural model when large deformation occurs.

In the proposed approach, fluid and solid particles share the same numerical nature and are treated within a unified ISPH framework, whereby a single system of equations is solved for both domains. The interaction between the fluid and the deformable walls is managed through an immersed formulation. Specifically, a computational domain is defined in which the deformable structures are directly embedded within the fluid, eliminating the need for explicit fluid–solid interface tracking. Within this immersed scheme, the fluid region surrounding the structure, referred to as the *buffer volume*, accommodates structural deformation. Owing to the absence of explicitly defined FSI interfaces, the method is fully meshless, both in the discretization of the two media and in their coupling. This feature circumvents a well-known limitation of partitioned FSI approaches, in which accurate treatment of the fluid–solid interface is required to ensure consistent and stable matching of the solutions across the two domains.

The method is three-dimensional and allows for handling complex geometries. However, for the clarity of representation, Fig. 1 illustrates a very simple 2D sketch considering a reference state [Fig. 1(a)] and a general deformed configuration [Fig. 1(b)]. As a first step, the whole computational domain is discretized with SPH particles that are categorized into three groups, depending on the domain in which they fall in the starting configuration. Particles lying inside the structural domain (whose boundaries are indicated with red lines in Fig. 1) are identified as *solid* (red dots in Fig. 1), and spring links are introduced among them. It should be noted that the boundaries of the structural domain serve only at the beginning, to identify *solid* particles in the reference configuration [Fig. 1(a)]. Subsequently, they evolve with the *solid* particle movement without requiring an explicit definition of

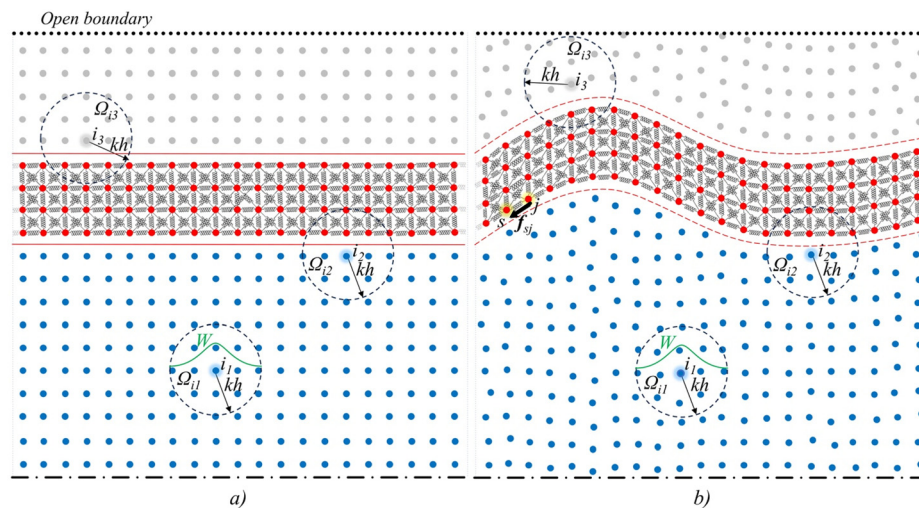


FIG. 1. 2D sketch of the immersed FSI numerical method in the reference (a) and deformed (b) configurations. Blue dots: effective fluid particles; red dots: solid particles; gray dots: reservoir fluid particles; dotted line: open boundary; red lines: reference (solid) and virtual deformed (dashed) structural boundaries.

their position [in Fig. 1(b), the deformed structural domains are sketched as dashed red lines only for clarity of representation]. Particles lying either inside the fluid or in the buffer regions are defined as *effective fluid* (blue dots) or *reservoir fluid* (gray dots), respectively. *Reservoir fluid* particles define a computational region of interest (CRoI) that accommodates the structural deformation and can enter and leave the computational domain through open boundaries (dotted lines) following the procedure described in Monteleone *et al.*⁸⁰

Particles interact with their neighbors, including those of different types, following the SPH formulation [Eq. (1)]. For instance, Fig. 1 highlights the support domain Ω of three particles (i_1, i_2, i_3): Ω_1 contains only *effective fluid* particles, Ω_2 encompasses both *effective fluid* and *solid*, Ω_3 includes both *solid* and *reservoir fluid* particles. It should be noted that, thanks to the absence of FSI interfaces, the current method is entirely meshless both in the treatment of the two media and in their coupling. Therefore, ghost particles are not required to handle fluid–solid interactions.

Springs connecting *solid* particles can be stretched or compressed, generating internal elastic forces that attempt to restore their resting length. In Fig. 1(b), the force f_{sj} between the *solid* particles s and j is indicated. The total internal force per unit mass, f_s , on each *solid* particle s can be expressed as a vector sum of the forces from all spring couplings it forms with its neighbors,

$$f_s = \frac{k_e h}{m_s} \sum_{j=1}^{N_s} (d_{0,sj} - d_{sj}) \hat{x}_{sj}, \quad (2)$$

where N_s is the total number of *solid* particles connected to s , k_e is the spring constant normalized over the *smoothing length* (h), $d_{0,sj}$ and d_{sj} are the resting and current spring lengths, respectively, and $\hat{x}_{sj} = (\mathbf{x}_s - \mathbf{x}_j)/d_{sj}$ is the unit vector directed from s to j . This total force is included in the momentum equations and thus integrated in the fractional-step scheme.⁷³ Specifically, it is added in the predictor-step equation as the mass force per unit mass. After calculating the updated velocity field, solid and fluid particles are moved at the end of each time step using the mean value of the new and old velocities.

The relationship between the spring constant and the Young’s modulus was determined from simulations of uniaxial tensile tests on a solid cube, as described in the work of Monteleone *et al.*⁷³

The pairs of *solid* particles linked by springs are defined at the beginning of the simulation [as shown in Fig. 1(a)] and maintained throughout the analysis. Therefore, while the support domain of the fluid particles changes as a result of the particle movement [i.e., particles i_1, i_2 , and i_3 in a general configuration, Fig. 1(b)], may have different neighbors from the reference state in Fig. 1(a)], each *solid* particle maintains the same list of neighboring *solid* particles in all configurations.

B. The proposed benchmark test case

To validate the immersed FSI method, a new three-dimensional benchmark test case was devised. Figure 2 shows a 3D visualization of the whole system [panel (a)] and a longitudinal cross section with the dimensions of the model [panel (b)].

The system consists of a cylindrical tube terminated by a hemispherical end-cap [hereafter referred to as the hemisphere-capped cylinder (HCC), and highlighted in red in Fig. 2(b)] made of an elastomeric deformable material, positioned coaxially around the nozzle at the distal end of a syringe. The cylindrical section of the HCC has an inner

diameter of 20 mm and a constant wall thickness of 2 mm, while the hemispherical end-cap has the same inner diameter as the tube but a variable wall thickness, increasing from 2 mm at the junction to 3 mm at the distal tip of the dome. The CAD model in *initial graphics exchange specification (.iges)* format is provided in [supplementary material 1](#).

To ensure optical access inside the HCC, the chamber was fabricated by injection molding, using Transil 40 silicone. This is a two-component platinum-cured room-temperature-vulcanizing (RTV) silicone rubber which, for thicknesses up to few millimeters, is optically clear.

The test fluid consisted of 75% propylene glycol (Carlo Erba Reagents) by volume, with the remaining 25% composed of phosphate-buffered saline (Sigma-Aldrich). This solution was specifically formulated to match the refractive index of the HCC material at room temperature, measured as $n=1.4095$ using an Optika Abbe bench refractometer. The selected test fluid has a density of $\rho_f = 1.0445$ g/ml and a dynamic viscosity of $\mu_f = 0.013478$ Pa s, measured using a peak hold test on a Discovery Hybrid Rheometer HR10 (TA Instruments, New Castle, DE, USA) at a shear rate of 10 s^{-1} , employing a stainless-steel conical geometry with a diameter of 60 mm and an angle of 2.016° . Since the HCC structure has inner and outer curved walls, the silicone chamber was enclosed within an external box with flat, transparent, parallel windows filled with the test fluid, in order to minimize optical distortions.^{94,95} The external box was 3D printed in black resin (Formlab) and closed with acrylic windows. A pipe, connected to an open tank exposed to the atmosphere, was incorporated to allow fluid to freely enter and exit the box, thereby accommodating the volume changes of the HCC. Figure 3 illustrates the deviation from rectilinear projection of a regular grid placed behind the external box–HCC system when filled with water [panel (a)] and with the test fluid [panel (b)]. The results clearly show that the selected setup effectively eliminates optical distortion, restoring the grid pattern.

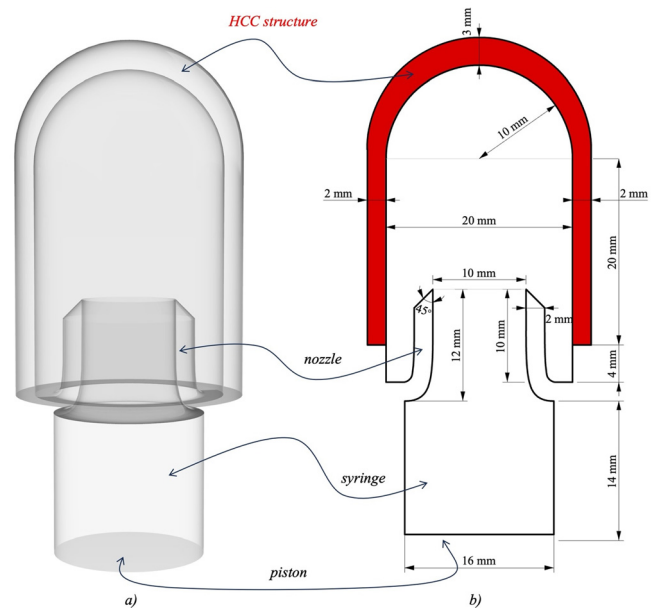


FIG. 2. Benchmark test: (a) 3D visualization; (b) longitudinal cross section of the geometry with dimensions.

25 March 2026 11:20:13

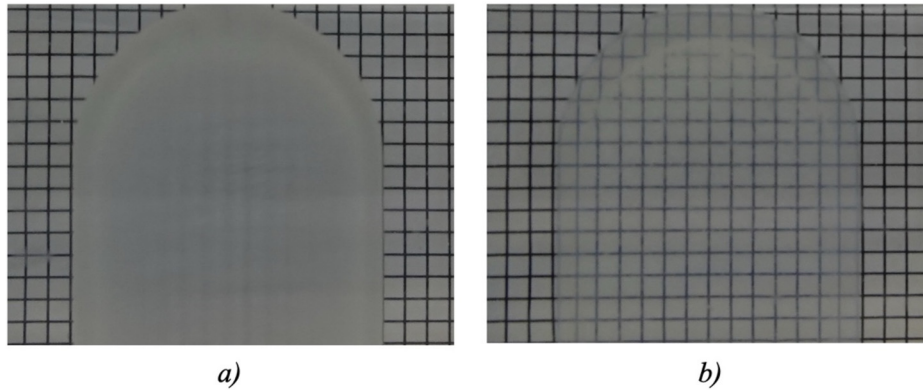


FIG. 3. Refractive index mismatch between the HCC model made in Transil 40 silicone and (a) water; (b) 75% propylene glycol solution.

The syringe, with an internal diameter of 16 mm, was operated by a syringe pump in cyclic reciprocating motion with a triangular waveform. The forward plunger stroke produced a 25% volume increase in the HCC (1.883 ml) over 5 s, corresponding to a flow rate of 22.60 ml/min; the return stroke used the same flow rate. To account for plunger seal elasticity, manufacturing tolerances, and syringe pump response, the effective syringe motion was measured experimentally by tracking the plunger flange with a camera using the *vision.PointTracker* algorithm in MATLAB. This yielded a period of $T = 10.476$ s and an effective flow rate of $Q = 27.62$ ml/min. Detailed syringe motion data are provided in [supplementary material 2](#) for reproducibility.

The liquid injected into the HCC induces a variation in the volume contained inside the chamber, and the presence of the central nozzle is expected to generate a vortex ring during the ejection.

Despite its simplicity, the system exhibits features common to complex cardiovascular models, such as large 3D strains of wall structures made from hyperelastic incompressible materials as a result of the interaction with dynamically pulsatile fluid flows.

The proposed benchmark was analyzed experimentally using particle image velocimetry (PIV) and modeled using the proposed immersed fluid–structure interaction (FSI) method. Despite the three-dimensional nature of both the experimental and numerical models, results comparison was conducted on a 2D diametral plane. This simplification is effective, considering that the test case is axisymmetric. Accordingly, a 2D-PIV measurement was performed on the same diametral plane from which the FSI numerical results were analyzed.

C. PIV analysis

Experimental analysis of the proposed benchmark was conducted using phase-resolved 2D-PIV, a non-intrusive optical technique that allows capturing velocity information of the whole flow field.⁹⁶ In brief, the fluid is seeded with small tracer particles, which are illuminated in a plane of interest with a laser sheet and acquired as pairs of images captured in rapid succession with a high-speed camera. The images in each couple are then compared using cross correlation algorithms, determining the flow parameters across the entire region of interest.

The experimental setup described above and used for the test is sketched in [Fig. 4](#).

Neutrally buoyant hollow glass spheres, 10 μm in diameter, were used to seed the fluid in the HCC chamber and syringe. Unseeded solution was used to fill the external box [through the red stopcock in

[Fig. 4\(a\)](#)] to ensure continuous refractive index matching. This outer fluid could flow into an external open chamber exposed to the atmosphere [see the syringe at the top of [Fig. 4\(a\)](#)] to allow free HCC expansion.

The PIV test was performed using a 2D phase-resolved TSI system, composed of a double-pulse Nd:YAG laser of 300 mW and wavelength of 532 nm, and a CCD camera with 2048×2048 square pixels and a frame rate of 15 Hz. The laser was connected to a collimator and a cylindrical lens of 15 mm, converting the laser beam into a light sheet approximately 1 mm thick. The camera and laser were synchronized with a laser-pulse synchronizer. The experiment was run projecting the laser sheet orthogonal to an external box window, along a sagittal symmetry plane of the HCC. The camera was placed orthogonal to the laser sheet, facing one of the adjacent external box windows. A photographic view of the experimental setup is provided in [Fig. 4\(b\)](#).

While the syringe pump was operating, 208 pairs of PIV images were acquired (each couple every 0.2 s) in the Insight 4 G software, with a time step of $\Delta t = 0.05$ s between pairs of images. These settings allow capturing three complete cycles, with over 50 image pairs per cycle.

PIV images were processed using Insight 4 G. After spatial calibration, a mask was applied to define the region of interest. A standard PIV algorithm was employed with the *image deformation* plugin, using the *fast Fourier transform* as the correlation engine and a *Gaussian peak* estimator.⁹⁷ The input images were first divided into interrogation regions (IRs) of 64×64 pixels to obtain an initial vector field. In a subsequent step, each IR was refined to 32×32 pixels and deformed to improve vector accuracy. Post-processing included a sequence of local validation steps and vector conditioning to ensure data quality. During local validation, vectors within a 5×5 IR neighborhood were compared to identify valid and invalid vectors. In the vector conditioning step, invalid vectors were removed and recursively replaced and smoothed using the surrounding valid vectors.

The resulting flow maps were then selected at characteristic time instants for comparison with corresponding numerical solutions.

D. Numerical setup

In the numerical simulation, the fluid was modeled as incompressible and Newtonian, with a density and dynamic viscosity as determined for the experimental liquid (described in [Sec. II C](#)).

[Figure 5](#) shows a schematic of the system with the different SPH particle types and the employed boundary conditions. As discussed in [Sec. II A](#), the computational domain is defined larger than the effective

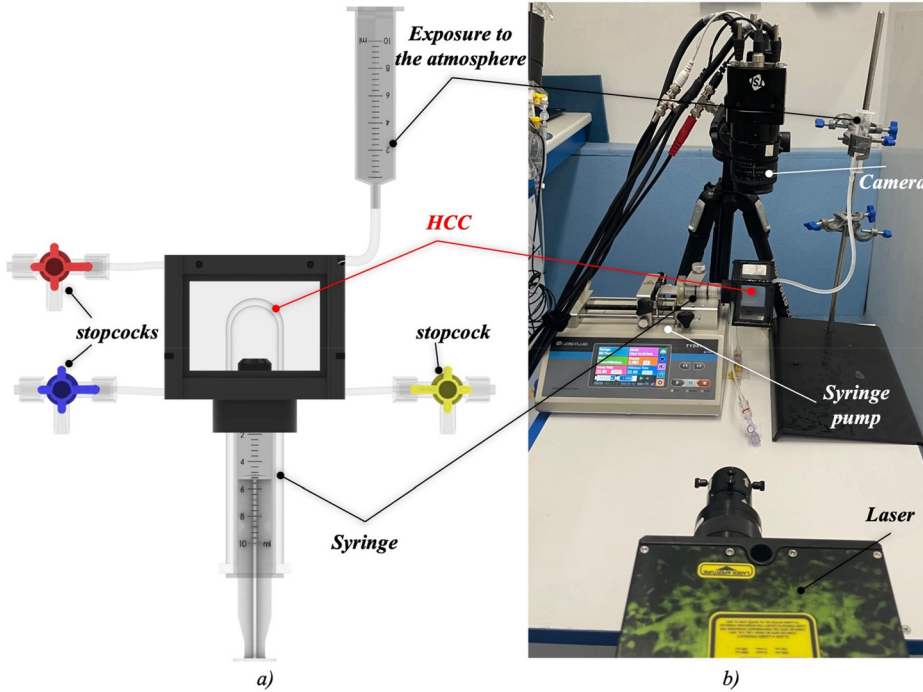


FIG. 4. (a) Sketch of the experimental model; (b) PIV setup.

domain dimensions (dimensions are provided in Fig. 2), so as to include a buffer volume of particles (*reservoir fluid* particles displayed as gray dots in Fig. 5), maintaining the deforming structure within the CRoI. The fluid domain, which includes the syringe and the liquid

volume within the HCC, is filled by *effective fluid* particles (depicted as blue dots in Fig. 5). *Solid* particles occupy the region of the deformable HCC structure (red dots in Fig. 5). An enlargement of the boxed region at the base of the HCC describes the boundary condition at the fixed region of the deformable structure. To this end, a flange of fixed *solid* particles (represented as white dots with red contour in Fig. 5) is defined, where the position is maintained throughout the simulation. For the fluid domain, adherence boundary condition with null velocity (black continuous lines) is imposed at fixed walls (syringe and nozzle walls). The displacement of the syringe (orange curve in the graph of Fig. 5), measured in the experimental test (see Sec. II C), is imposed at the syringe plunger using adherence condition with the moving boundary (orange line in the sketch of Fig. 5).

A constant null pressure value is imposed at the open boundary of the buffer domain (dotted black line), allowing *reservoir fluid* particles to enter/exit, allowing the structure deformation following the procedure described in Monteleone *et al.*⁸⁰

In the simulation, a *smoothing length*, h , equal to 0.4 mm is used, corresponding to an initial total number of particles equal to 453 214 (subdivided as 187 793; 84 616; and 180 805; for the fluid, the structure, and the buffer domains, respectively). This value was selected based on a particle-resolution study, considering three smoothing lengths (0.67, 0.5, and 0.4 mm). Given the small differences in structural wall displacement and velocity profiles, $h = 0.4$ mm was chosen to maintain a particle density consistent with the PIV experiment. To ensure stability within the explicit integration scheme, the time step was determined by two primary constraints. First, it satisfied the Courant–Friedrichs–Lewy (CFL) condition for SPH: $\Delta t_{CFL} \leq \lambda_v (h/u_{max})$, where u_{max} is the maximum particle velocity magnitude and $\lambda_v = 0.4$.⁹⁸ Additionally, the time step was limited by the maximum force magnitude experienced by the springs (f_{max}),

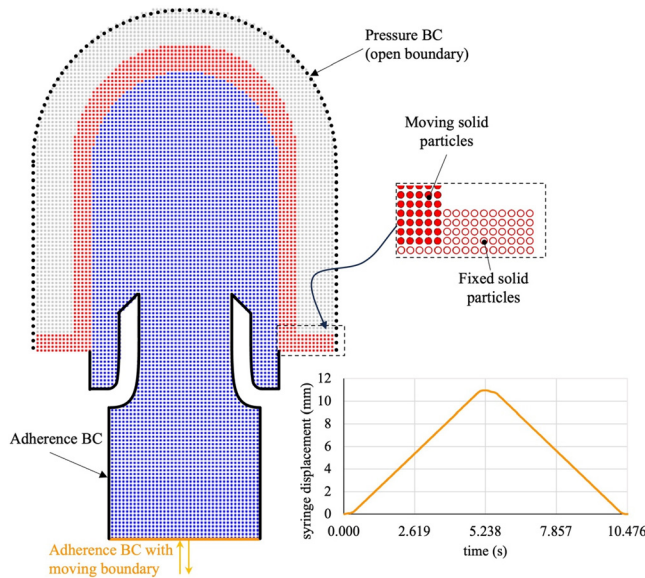


FIG. 5. Sketch of the boundary conditions and SPH particle types in the proposed HCC benchmark (at the undeformed reference configuration). Blue dots: effective fluid particles; red dots: deformed solid particles; white dots with red contour: fixed solid particles; gray dots: reservoir fluid particles.

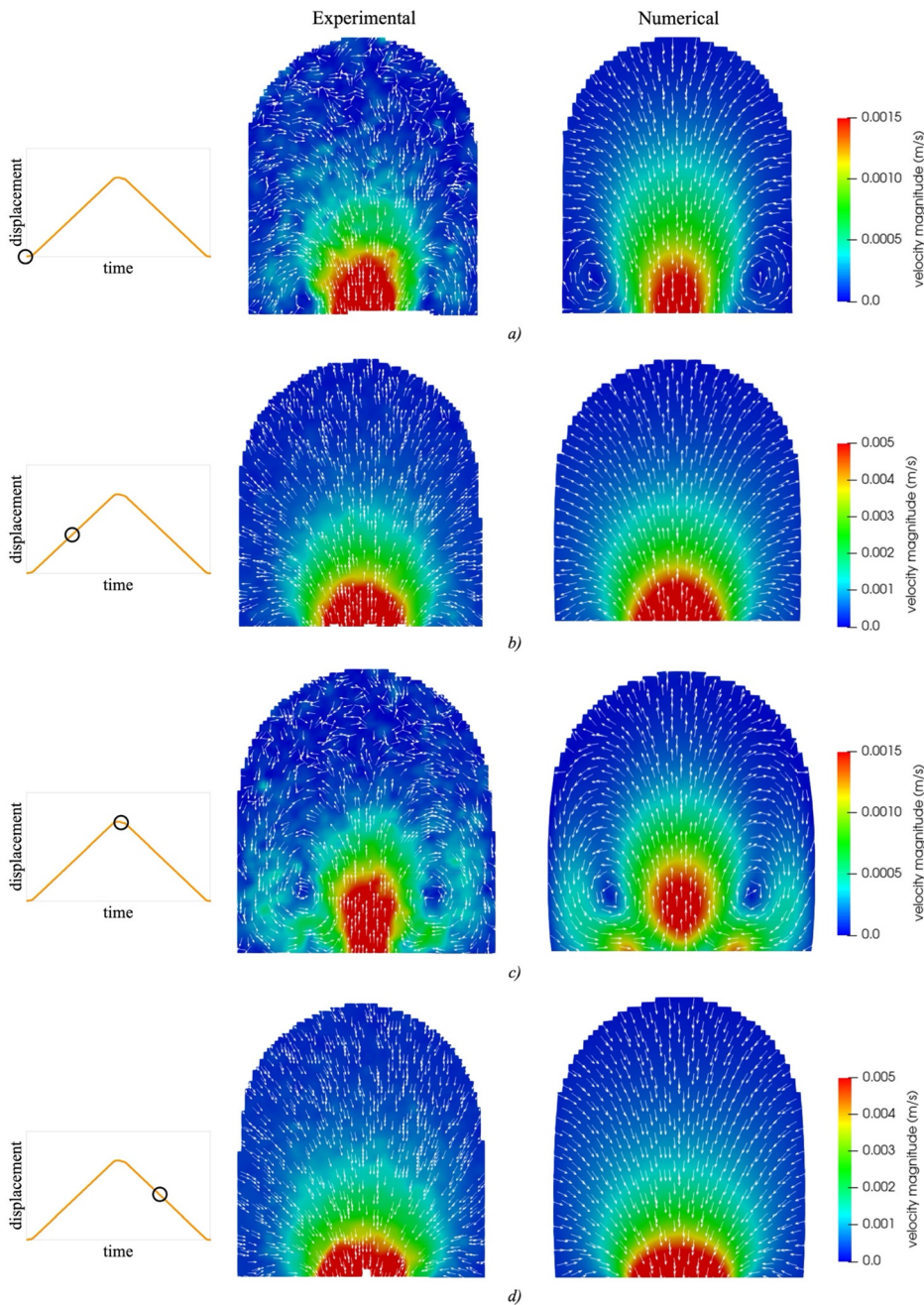


FIG. 6. Experimental (left column) and numerical (right column) velocity maps at four time instants: (a) minimum stroke; (b) half stroke forward, (c) direction inversion at the maximum stroke; (d) half stroke back.

defined as $\Delta t_f \leq \lambda_f \left(\sqrt{h/f_{max}} \right)$,^{99,100} where λ_f is a constant factor set equal to 0.25.^{98,100} Based on these conditions, a time step of $\Delta t = 0.002$ s was employed in the simulation. Three consecutive piston strokes were performed, verifying that the periodicity was reached at the second cycle.

The simulation was carried out on an AMD EPYC GHz processor with two sockets and 24 cores per socket. The central processing unit (CPU) wall-clock time spent to advance the solution in

time in serial mode is about 32 s (thus, 46.5 h is required to simulate a whole period with the employed time step). Future development will be aimed at reducing computational costs, extending the parallelization algorithm of Monteleone *et al.*¹⁰¹

III. RESULTS AND DISCUSSION

Four characteristic time instants were selected to analyze and compare numerical and experimental results in terms of fluid velocity

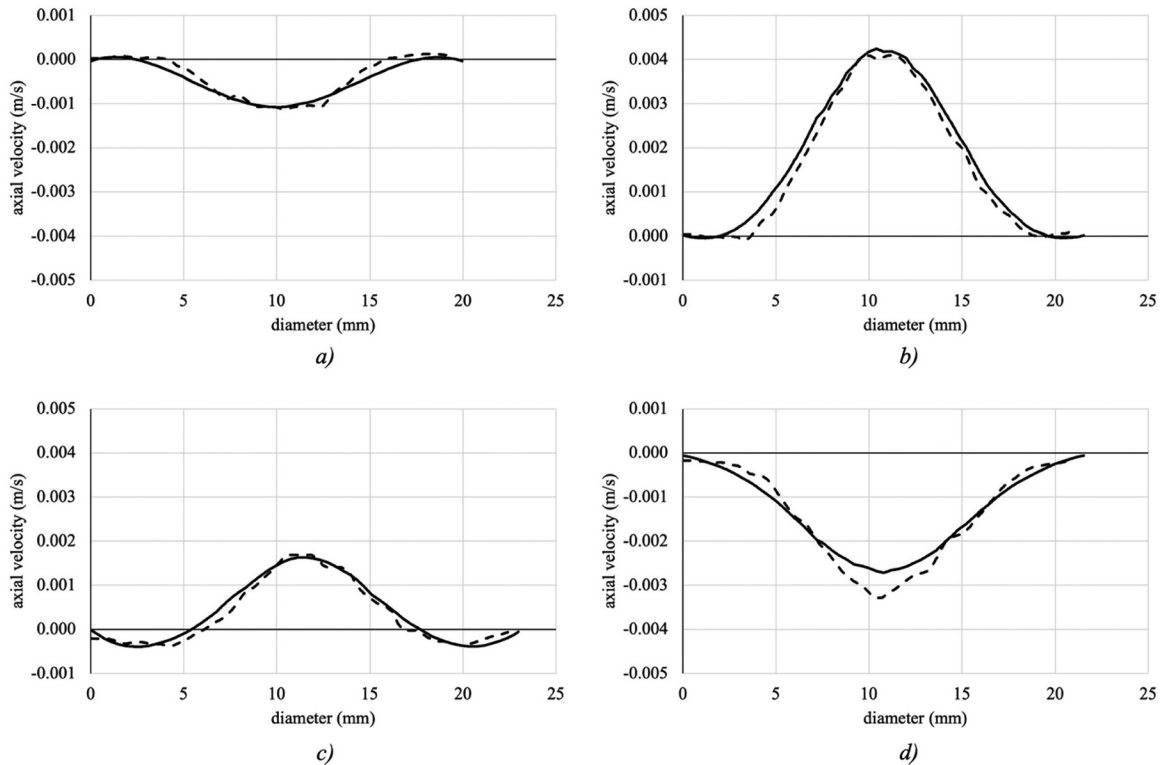


FIG. 7. Comparison of velocity profile between experimental (dashed lines) and numerical (continuous lines) results at four time instants: (a) minimum stroke; (b) half stroke forward; (c) inversion at the maximum stroke; and (d) half stroke back.

and structural deformation. Specifically, the bottom dead center (BDC), the top dead center (TDC), and the two intermediate instants at the middle of the forward and return strokes were selected. The numerical results were analyzed at the second cycle, as it was verified that the periodicity had already been reached.

Figure 6 shows the experimental and numerical velocity maps (left and right columns, respectively) at the analyzed instants. Velocity vectors are represented in white, with constant length. For clarity, the velocity scale used at the dead centers [Figs. 6(a) and 6(c)], when the flow inversion is associated with slower flow dynamics, range between 0 and 1.5 mm/s; while the instant at half strikes, characterized by faster motion [Figs. 6(b) and 6(d)], is represented in a velocity scale ranging from 0 to 5 mm/s and when it proceeds with constant velocity.

At the BDC [see Fig. 6(a)], the velocity is maximum at the exit of the nozzle, and drops close to the HCC wall. This region is characterized by the lowest velocities observed during the cycle and is, therefore, associated with the largest experimental errors.^{102,103} Moreover, the clear vortex ring observed in the numerical results is only partially visible in the PIV analysis due to its proximity to the lower mask edges.

During the forward stroke [see Fig. 6(b)], fluid is pushed into the HCC, which expands. At this instant, velocity vectors are significantly higher in magnitude and reversed in direction with respect to the BDC instant, showing a fast jet at the nozzle exit progressively reducing toward the chamber walls.

At the TDC [see Fig. 6(c)], both numerical and experimental maps show a velocity peak of about 1.5 mm/s still directed toward the hemisphere, but now above the nozzle (where the mean velocity becomes negligible). This is accompanied by a concentric vortex ring, clearly observable in both studies.

In the return stroke [see Fig. 6(d)], the velocity fields exhibit characteristics analogous to the respective forward case [see Fig. 6(b)], but with inverted vectors direction (these are now directed toward the nozzle), and slightly flatter in magnitude, a consequence of the increased fluidic resistance encountered during the passage of the flow from the HDC volume into the nozzle.

The velocity maps presented in Fig. 6 demonstrate close agreement between experimental and numerical outcomes.

To enable a more quantitative comparison, velocity profiles were extracted at all analyzed instants along a diameter located 6 mm above the nozzle, corresponding to the center of the vortex ring generated at TDC [Fig. 6(c)]. The resulting profiles are shown in Fig. 7. The experimental standard uncertainty of the selected velocity profile was evaluated at a 68% confidence level, representing the interval within which the true velocity values are expected to lie.^{97,104} The mean standard uncertainty bound of each profile was compared with the mean velocity magnitude in the central 50% of the velocity profiles. The uncertainty bound of the velocity profiles ranged from 4% to 16% of the mean velocity magnitude.

Excellent agreement was observed between the numerical and experimental curves across all instants, with the maximum percentage

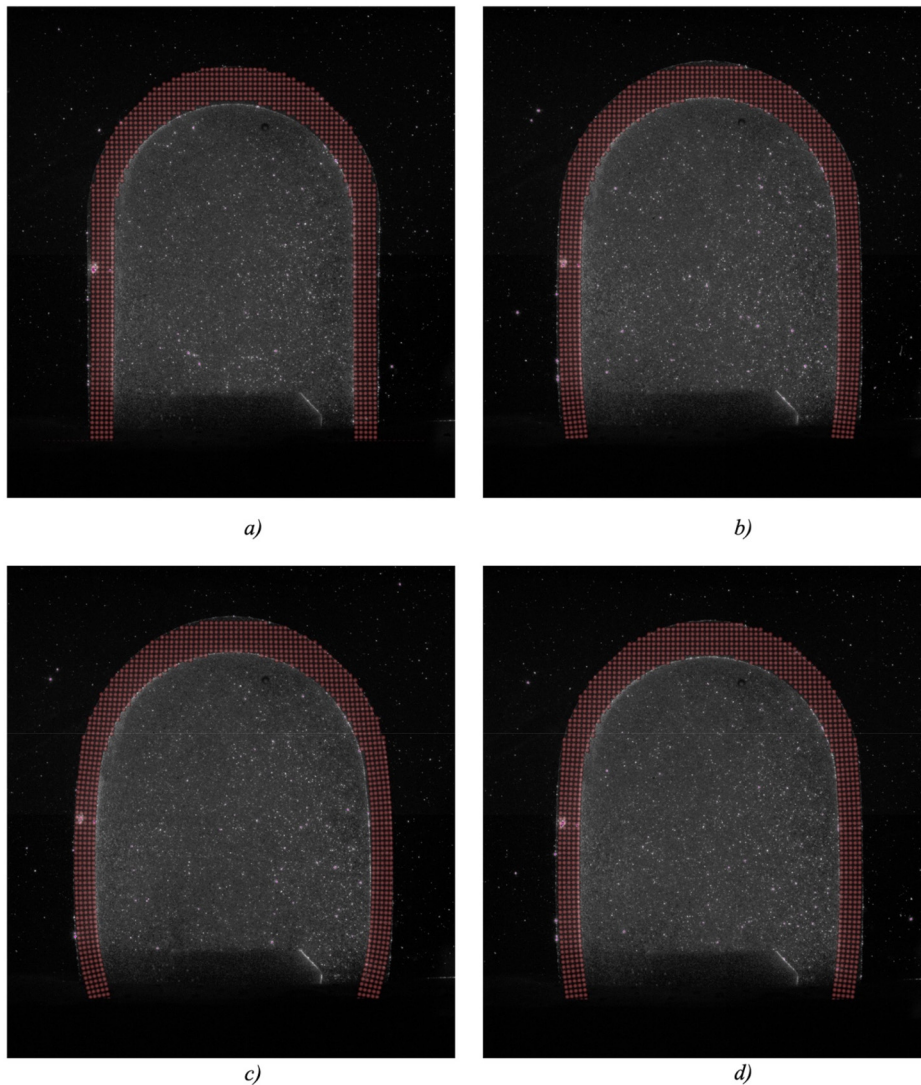


FIG. 8. Comparison of the HCC deformation between experimental (PIV images) and numerical (red points) results at four time instants: (a) minimum stroke; (b) half stroke forward; (c) inversion at the maximum stroke; and (d) half stroke back.

difference of 11%, occurring at mid return stroke [Fig. 7(d)]. This value was calculated as the mean absolute relative error of the numerical result with respect to the experimental data within the central 50% of the velocity profiles.

Furthermore, the deformation of the HCC walls was assessed. Figure 8 shows the solid particles (red dots) superimposed on the raw PIV images at the selected instants. As the HCC volume increases by 25%, the numerically predicted wall deformation closely matches the experimental observations at all instants, confirming excellent agreement. The video of the numerical results vs experimental images of one cycle is made available in [supplementary material 3](#).

The diameter variation ($\Delta D/D$) measured at the midpoint of the HCC cylindrical region [see Fig. 9(a)] is reported in Fig. 9(b), showing good agreement between experimental (dashed line) and numerical (solid line) results. Both experimental and computational outcomes

achieve a peak variation of about 14%, exhibiting a mean variation difference below 5%.

The proposed benchmark, simple to implement both experimentally and numerically, successfully reproduced a highly deformable chamber with curved walls interacting with a pulsatile flow. The resulting flow field was characterized by the formation of vortex rings during flow reversals [see Figs. 6(a) and 6(c)], a hydrodynamic feature valuable for quantitative experimental validations. This setup therefore provides a simplified yet representative emulation of hemodynamic conditions occurring in complex cardiovascular scenarios, such as the filling and emptying of the left atrial appendage—an anatomical protrusion of the left atrium extensively investigated through computational approaches due to its elevated thromboembolic risk.^{8,34,79,105–107}

This benchmark may then serve as a practical reference for validating computational methods in cardiovascular scenarios,

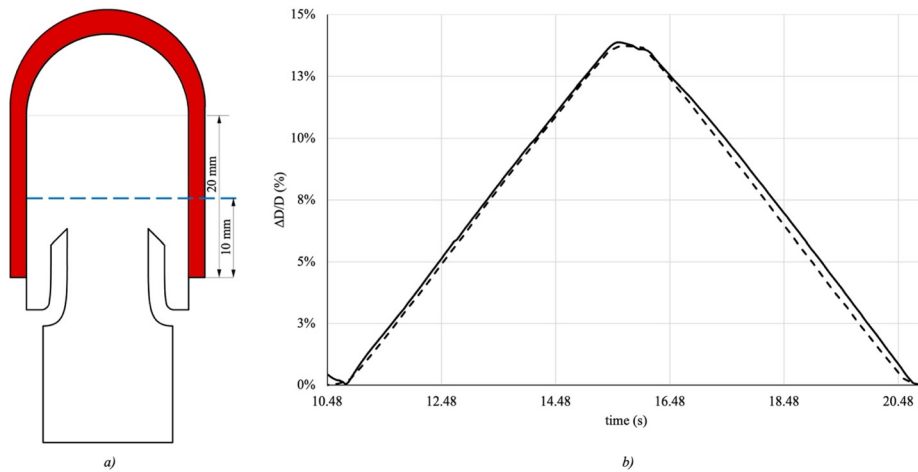


FIG. 9. (a) Longitudinal cross section of the geometry with indication of the location of the diameter measurement (dashed blue line); (b) comparison of the HCC diameter variation ($\Delta D/D$) during the second cycle. Experimental (dashed line) and numerical (continuous line) results.

which are often assessed by comparison with other numerical approaches.^{108–111}

The proposed immersed FSI approach proved highly effective in simulating these scenarios, as demonstrated by the strong agreement between numerical and experimental results (Figs. 6–9). A key advantage of the proposed method lies in its fully meshless nature, which eliminates the need for explicit FSI interface definitions and enables the use of a unified physical formulation for both fluid and solid phases. Within this framework, the shared fluid–structure computational domain prevents truncation of the kernel support and avoids particle penetration at the interface, without requiring additional corrective algorithms that would otherwise increase computational cost and methodological complexity. Crucially, this approach effectively addresses a long-standing challenge of boundary treatment in SPH methods, which often necessitates the introduction of mirror or ghost particles to enforce interface conditions.^{58,63,64,68,69}

This experimentally validated immersed FSI approach could be used in several cardiovascular applications characterized by complex patient-specific geometry and large deformation, e.g., to simulate the deformation of the left atrial appendage or the formation and effect of aneurysms.

Furthermore, the proposed FSI approach could be highly valuable in hybrid techniques, such as EMRI,⁸⁵ which aim to correct 4D flow MRI data with numerical filtering. Its key advantage in this context is that it does not require any mesh definition or time-dependent mesh updates, a major bottleneck for the application of such procedures to patient-specific geometries with moving walls.¹¹²

Some limitations of the proposed FSI method should be noted. In particular, it requires the use of uniform discretization for both fluid and structural domains, meaning that the modeling of thin structures dictates the choice of the *smoothing length* value, which can lead to a large number of particles in specific problems. This issue, however, can be substantially mitigated by employing procedures already implemented for the same code, such as parallelization schemes¹⁰¹ or multi-domain techniques.⁸⁸ Additionally, the material is modeled as incompressible, with density equal to that of the fluid, due to the employed ISPH approach. Although this assumption is effective for cardiovascular soft tissues^{76,77} (and for elastomers such as the silicone employed in this study), it may not be applicable to synthetic biomaterials

commonly used in prosthetic devices. The model is based on a basic description of the material constitutive laws, which currently does not model nonlinearity, viscoelasticity and anisotropy. The implementation of nonlinear strain-energy responses, viscoelastic, and anisotropic behaviors represents a planned future development. A further concern is tensile instability, which induces particle clumping during computation and has consequently become one of the major barriers to the broader adoption of SPH in practical applications.^{92,93} As mentioned in Sec. II A, this work employs the shifting procedure proposed by Xu *et al.*⁹⁰ to ensure a more uniform particle distribution throughout the simulation. While this procedure mitigates the issue, tensile instability can still lead to numerical instability and unreliable results in long simulations (e.g., if a large number of cycles are required to achieve periodicity). Moreover, although the shifting procedure is essential in ISPH simulation,¹¹³ it could introduce physical inaccuracies.

Finally, as mentioned in the Introduction, the present approach has already been successfully used to model thrombus formation, where convection-diffusion equations were included to model the evolution of biochemical species of the coagulative cascade.^{78,79} These could be adapted in future studies, including reaction terms to model electrophysiology effects.

IV. CONCLUSIONS

An entirely meshless FSI approach is presented for modeling cardiovascular problems. The method is based on the ISPH algorithm and uses a unified physics framework to represent both fluid and structure. Structure is handled by linking SPH particles via spring laws, leading to an implicit FSI coupling where both fluid and solid particles are solved together in the same system. This overcomes a well-known FSI challenge related to the handling of fluid–solid interfaces. The absence of FSI interfaces is in fact a key advantage of this approach, making the method entirely meshless. This feature greatly simplifies the handling of large deformations and complex geometries inherent in cardiovascular simulations.

A key aspect of the present work is the rigorous experimental validation of the proposed FSI method. To this end, a novel benchmark test was introduced, designed to facilitate experimental validation while remaining highly relevant for modeling complex cardiovascular phenomena. Despite its simplified geometry, the benchmark captures

essential features present in physiological hemodynamics problems, including pulsatile flow, deformable curved walls, high three-dimensional strain, and large volume variation during alternating filling and emptying phases. The experimental investigations were conducted using the PIV technique, widely recognized as the gold standard for *in vitro* flow analysis. Reference data of the benchmark, such as geometry, boundary conditions, and experimental results, are shared to enable the scientific community to validate FSI computational approaches vs relevant experimental data.

The comparative analysis of numerical and experimental results demonstrated a very good match in both velocity fields and structural deformation. The experimentally validated FSI tool enables obtaining reliable numerical simulations in the cardiovascular framework and could be used in the future to provide deeper insights into blood and soft-tissue dynamic interaction and cardiovascular diseases.

SUPPLEMENTARY MATERIAL

See the [supplementary material](#) for the following: (1) fluid and structural geometries of the FSI benchmark; (2) experimental syringe displacement used as a boundary condition of the numerical FSI benchmark; and (3) video of the numerical results vs experimental images.

ACKNOWLEDGMENTS

Part of this work was carried out with the financial support of the Regione Siciliana under Project Nos. 2021.IT.05.SFPR.014/002/04.7/09.02.03/A15_24/0001 (CIP), G71I24000280006 (CUP), and DR 11689/2024.

AUTHOR DECLARATIONS

Conflict of Interest

The authors have no conflicts to disclose.

Author Contributions

Alessandra Monteleone and Sofia Di Leonardo contributed equally to this paper.

Alessandra Monteleone: Conceptualization (equal); Data curation (equal); Formal analysis (equal); Investigation (equal); Methodology (equal); Software (equal); Validation (equal); Visualization (equal); Writing – original draft (equal). **Sofia Di Leonardo:** Conceptualization (equal); Data curation (equal); Formal analysis (equal); Investigation (equal); Methodology (equal); Validation (equal); Visualization (equal); Writing – original draft (equal). **Marco Correnti:** Data curation (equal); Formal analysis (equal); Investigation (equal); Methodology (equal); Validation (equal); Visualization (equal); Writing – review & editing (equal). **Giorgio Micale:** Funding acquisition (equal); Resources (equal); Supervision (equal); Visualization (equal); Writing – review & editing (equal). **Gaetano Burriesci:** Conceptualization (equal); Data curation (equal); Formal analysis (equal); Funding acquisition (equal); Investigation (equal); Methodology (equal); Project administration (equal); Resources (equal); Supervision (equal); Validation (equal); Visualization (equal); Writing – review & editing (equal).

DATA AVAILABILITY

The data that support the findings of this study are available within the article and its [supplementary material](#).

REFERENCES

- ¹S. Schoenborn, S. Pirola, M. A. Woodruff, and M. C. Allenby, “Fluid-structure interaction within models of patient-specific arteries: Computational simulations and experimental validations,” *IEEE Rev. Biomed. Eng.* **17**, 280–296 (2024).
- ²R. Pramanik, R. W. C. P. Verstappen, and P. R. Onck, “Computational fluid–structure interaction in biology and soft robots: A review,” *Phys. Fluids* **36**, 101302 (2024).
- ³O. Powar, P. A. H. Arun, A. M. Kumar, M. Kanchan, B. M. Karthik, P. Mangalore, and M. Santhya, “Recent developments in the immersed boundary method for complex fluid–structure interactions: A review,” *Fluids* **10**, 134 (2025).
- ⁴D. E. Bloom, E. Cafiero, E. Jané-Llopis, S. Abrahams-Gessel, L. R. Bloom, S. Fathima, A. B. Feigl, T. Gaziano, A. Hamandi, M. Mowafi, D. O’Farrell, E. Ozaltin, A. Pandya, K. Prettnner, L. Rosenberg, B. Seligman, A. Z. Stein, C. Weinstein, and J. Weiss, “The global economic burden of noncommunicable diseases,” Program on the Global Demography of Aging: PGDA Working Paper No. 8712, 2012.
- ⁵A. Athani, N. N. N. Ghazali, I. A. Badruddin, A. Y. Usmani, M. Amir, D. Singh, and S. H. Khan, “Image-based hemodynamic and rheological study of patient’s diseased arterial vasculatures using computational fluid dynamics (CFD) and fluid–structure interactions (FSI) analysis: A review,” *Arch. Comput. Methods Eng.* **32**, 1427–1457 (2025).
- ⁶M. Hirschhorn, V. Tchantchaleishvili, R. Stevens, J. Rossano, and A. Throckmorton, “Fluid–structure interaction modeling in cardiovascular medicine – A systematic review 2017–2019,” *Med. Eng. Phys.* **78**, 1–13 (2020).
- ⁷A. M. Tango, J. Salmons-Smith, A. Ducci, and G. Burriesci, “Validation and extension of a fluid–structure interaction model of the healthy aortic valve,” *Cardiovasc. Eng. Technol.* **9**, 739–751 (2018).
- ⁸G. Musotto, A. Monteleone, D. Vella, B. Zuccarello, R. Cannova, A. Cook, G. M. Bosi, and G. Burriesci, “Fluid–structure interaction analysis of the thromboembolic risk in the left atrial appendage under atrial fibrillation: Effect of hemodynamics and morphological features,” *Comput. Methods Programs Biomed.* **246**, 108056 (2024).
- ⁹M. I. Afridi, M. Izadi, M. Eizadi, H. A. Mohammed, R. Karimi, F. Alqurashi, M. H. Mohamed, A. Hajar, M. B. Ben Hamida, I. Mahariq, and S. Rahimi, “Fluid–structure interaction in engineering based on its applications: A planetary and up-to-date review,” *Phys. Fluids* **36**, 101309 (2024).
- ¹⁰K. D. Lau, V. Diaz-Zuccarini, P. Scambler, and G. Burriesci, “Fluid–structure interaction study of the edge-to-edge repair technique on the mitral valve,” *J. Biomech.* **44**, 2409–2417 (2011).
- ¹¹R. Jayendiran, B. Nour, and A. Ruimi, “Fluid–structure interaction (FSI) analysis of stent-graft for aortic endovascular aneurysm repair (EVAR): Material and structural considerations,” *J. Mech. Behav. Biomed. Mater.* **87**, 95–110 (2018).
- ¹²J. De Hart, G. W. M. Peters, P. J. G. Schreurs, and F. P. T. Baaijens, “A three-dimensional computational analysis of fluid–structure interaction in the aortic valve,” *J. Biomech.* **36**, 103–112 (2003).
- ¹³A. Laadhari and G. Székely, “Eulerian finite element method for the numerical modeling of fluid dynamics of natural and pathological aortic valves,” *J. Comput. Appl. Math.* **319**, 236–261 (2017).
- ¹⁴A. M. Tango, A. Ducci, and G. Burriesci, “*In silico* study of the ageing effect upon aortic valves,” *J. Fluids Struct.* **103**, 103258 (2021).
- ¹⁵A. P. Yoganathan, K. B. Chandran, and F. Sotiropoulos, “Flow in prosthetic heart valves: State-of-the-art and future directions,” *Ann. Biomed. Eng.* **33**, 1689–1694 (2005).
- ¹⁶S. S. Abbas, M. S. Nasif, and R. Al-Waked, “State-of-the-art numerical fluid–structure interaction methods for aortic and mitral heart valves simulations: A review,” *Simulation* **98**, 3–34 (2022).
- ¹⁷D. Oks, C. Samaniego, G. Houzeaux, C. Butakoff, and M. Vázquez, “Fluid–structure interaction analysis of eccentricity and leaflet rigidity on thrombosis

- biomarkers in bioprosthetic aortic valve replacements,” *Int. J. Numer. Methods Biomed. Eng.* **38**, e3649 (2022).
- ¹⁸K.-M. Bornemann, S. E. Jahren, and D. Obrist, “The relation between aortic morphology and transcatheter aortic heart valve thrombosis: Particle tracing and platelet activation in larger aortic roots with and without neo-sinus,” *Comput. Biol. Med.* **179**, 108828 (2024).
- ¹⁹O. Mutlu, M. Saribay, M. M. Yavuz, H. E. Salman, A. Al-Nabti, and H. C. Yalcin, “Material modeling and recent findings in transcatheter aortic valve implantation simulations,” *Comput. Methods Programs Biomed.* **255**, 108314 (2024).
- ²⁰A. M. Tango, A. Monteleone, A. Ducci, and G. Burriesci, “Analysis of the haemodynamic changes caused by surgical and transcatheter aortic valve replacements by means fluid-structure interaction simulations,” *Comput. Biol. Med.* **186**, 109673 (2025).
- ²¹M. Fandaros, C. Kwok, Z. Wolf, N. Labropoulos, and W. Yin, “Patient-specific numerical simulations of coronary artery hemodynamics and biomechanics: A pathway to clinical use,” *Cardiovasc. Eng. Technol.* **15**, 503–521 (2024).
- ²²A. A. Ekmejian, H. J. Carpenter, J. L. Ciofani, B. H. M. Gray, U. K. Allahwala, M. Ward, J. Escaned, P. J. Psaltis, and R. Bhandi, “Advances in the computational assessment of disturbed coronary flow and wall shear stress: A contemporary review,” *J. Am. Heart Assoc.* **13**, e037129 (2024).
- ²³Y. He, H. Northrup, H. Le, A. K. Cheung, S. A. Berceci, and Y. T. Shiu, “Medical image-based computational fluid dynamics and fluid-structure interaction analysis in vascular diseases,” *Front. Bioeng. Biotechnol.* **10**, 855791 (2022).
- ²⁴A. A. Rostam-Alilou, H. R. Jarrah, A. Zolfagharian, and M. Bodaghi, “Fluid-structure interaction (FSI) simulation for studying the impact of atherosclerosis on hemodynamics, arterial tissue remodeling, and initiation risk of intracranial aneurysms,” *Biomech. Model. Mechanobiol.* **21**, 1393–1406 (2022).
- ²⁵C. Zhao, R. Lv, A. Maehara, L. Wang, Z. Gao, Y. Xu, X. Guo, Y. Zhu, M. Huang, X. Zhang, J. Zhu, B. Yu, H. Jia, G. S. Mintz, and D. Tang, “Plaque ruptures are related to high plaque stress and strain conditions: Direct verification by using *in vivo* OCT rupture data and FSI models,” *Arterioscler., Thromb., Vasc. Biol.* **44**, 1617–1627 (2024).
- ²⁶A. Balasubramanya, L. Gheysen, M. U. Wagenhäuser, N. Famaey, J. Degroote, and P. Segers, “Hemodynamics in aortic dissections: A fluid-solid interaction study in an idealized dissection model with a false lumen side branch,” *J. Biomech.* **188**, 112771 (2025).
- ²⁷E. S. Di Martino, G. Guadagni, A. Fumero, G. Ballerini, R. Spirito, P. Biglioli, and A. Redaelli, “Fluid-structure interaction within realistic three-dimensional models of the aneurysmatic aorta as a guidance to assess the risk of rupture of the aneurysm,” *Med. Eng. Phys.* **23**, 647–655 (2001).
- ²⁸M. Xenos, S. H. Rambhia, Y. Alemu, S. Einav, N. Labropoulos, A. Tassiopoulos, J. J. Ricotta, and D. Bluenstein, “Patient-based abdominal aortic aneurysm rupture risk prediction with fluid structure interaction modeling,” *Ann. Biomed. Eng.* **38**, 3323–3337 (2010).
- ²⁹J. Fonken, T. Timmer, A. Nievergeld, M. Thirugnanasambandam, M. van Sambeek, F. van de Vosse, and R. Lopata, “Longitudinal ultrasound-based fluid-structure interaction study on hemodynamics and wall mechanics in abdominal aortic aneurysms,” *Comput. Biol. Med.* **195**, 110486 (2025).
- ³⁰A. Valencia, P. Burdiles, M. Ignat, J. Mura, E. Bravo, R. Rivera, and J. Sordo, “Fluid structural analysis of human cerebral aneurysm using their own wall mechanical properties,” *Comput. Math. Methods Med.* **2013**, 293128.
- ³¹R. Razaghi, H. Biglari, and A. Karimi, “Risk of rupture of the cerebral aneurysm in relation to traumatic brain injury using a patient-specific fluid-structure interaction model,” *Comput. Methods Programs Biomed.* **176**, 9–16 (2019).
- ³²X. Wang and X. Huang, “Risk factors and predictive indicators of rupture in cerebral aneurysms,” *Front. Physiol.* **15**, 1454016 (2024).
- ³³A. K. Alagan, C. Valeti, S. Bolem, O. S. Karve, K. R. Arvind, P. Rajalakshmi, A. Sabareeswaran, S. Gopal, G. Matham, H. R. Darshan, B. J. Sudhir, and B. S. V. Patnaik, “Histopathology-based near-realistic arterial wall reconstruction of a patient-specific cerebral aneurysm for fluid-structure interaction studies,” *Comput. Biol. Med.* **185**, 109579 (2025).
- ³⁴G. Musotto, A. Monteleone, D. Vella, S. Di Leonardo, A. Viola, G. Pitarresi, B. Zuccarello, A. Pantano, A. Cook, G. M. Bosi, and G. Burriesci, “The role of patient-specific morphological features of the left atrial appendage on the thromboembolic risk under atrial fibrillation,” *Front. Cardiovasc. Med.* **9**, 894187 (2022).
- ³⁵K. K. L. Wong, P. Thavornpattanaong, S. C. P. Cheung, and J. Tu, “Numerical stability of partitioned approach in fluid-structure interaction for a deformable thin-walled vessel,” *Comput. Math. Methods Med.* **2013**, 631719.
- ³⁶A. Cetin and M. Sahin, “A monolithic fluid-structure interaction framework applied to red blood cells,” *Int. J. Numer. Methods Biomed. Eng.* **35**, e3171 (2019).
- ³⁷S. T. Ha, L. C. Ngo, M. Saeed, B. J. Jeon, and H. Choi, “A comparative study between partitioned and monolithic methods for the problems with 3D fluid-structure interaction of blood vessels,” *J. Mech. Sci. Technol.* **31**, 281–287 (2017).
- ³⁸A. G. Kuchumov, V. Vedeneev, V. Samartsev, A. Khairulin, and O. Ivanov, “Patient-specific fluid-structure interaction model of bile flow: Comparison between 1-way and 2-way algorithms,” *Comput. Methods Biomech. Biomed. Eng.* **24**, 1693–1717 (2021).
- ³⁹D. Forti, M. Bukac, A. Quaini, S. Canic, and S. Deparis, “A monolithic approach to fluid-composite structure interaction,” *J. Sci. Comput.* **72**, 396–421 (2017).
- ⁴⁰J. Donea, S. Giuliani, and J. P. Halleux, “An arbitrary Lagrangian-Eulerian finite element method for transient dynamic fluid-structure interactions,” *Comput. Methods Appl. Mech. Eng.* **33**, 689–723 (1982).
- ⁴¹M. Souli, A. Ouahsine, and L. Lewin, “ALE formulation for fluid-structure interaction problems,” *Comput. Methods Appl. Mech. Eng.* **190**, 659–675 (2000).
- ⁴²E. Kuhl, S. Hulshoff, and R. de Borst, “An arbitrary Lagrangian Eulerian finite-element approach for fluid-structure interaction phenomena,” *Int. J. Numer. Methods Eng.* **57**, 117–142 (2003).
- ⁴³C. S. Peskin, “The immersed boundary method,” *Acta Numer.* **11**, 479–517 (2002).
- ⁴⁴I. Borazjani, “Fluid-structure interaction, immersed boundary-finite element method simulations of bio-prosthetic heart valves,” *Comput. Methods Appl. Mech. Eng.* **257**, 103–116 (2013).
- ⁴⁵B. E. Griffith and N. A. Patankar, “Immersed methods for fluid-structure interaction,” *Annu. Rev. Fluid Mech.* **52**, 421–448 (2020).
- ⁴⁶V. K. Srivastav, S. Thota, L. M. Kumar, and A. R. Anand, “Interface problems-fluid structure interaction: Description, application and review,” *WSEAS Trans. Biol. Biomed.* **21**, 218–226 (2024).
- ⁴⁷F. Duarte, R. Gormaz, and S. Natesan, “Arbitrary Lagrangian-Eulerian method for Navier-Stokes equations with moving boundaries,” *Comput. Methods Appl. Mech. Eng.* **193**, 4819–4836 (2004).
- ⁴⁸W. Mao, A. Caballero, R. McKay, C. Primiano, and W. Sun, “Fully-coupled fluid-structure interaction simulation of the aortic and mitral valves in a realistic 3D left ventricle model,” *PLoS One* **12**, e0184729 (2017).
- ⁴⁹C. Ruan, J. Zhou, Z. Zhang, T. Li, L. Chen, Z. Li, and Y. Chen, “Numerical simulation progress of whole-heart modeling: A review,” *Phys. Fluids* **36**, 111301 (2024).
- ⁵⁰C. S. Peskin, “Flow patterns around heart valves: A numerical method,” *J. Comput. Phys.* **10**, 252–271 (1972).
- ⁵¹G. Marom, “Numerical methods for fluid-structure interaction models of aortic valves,” *Arch. Comput. Methods Eng.* **22**, 595–620 (2015).
- ⁵²A. M. Bavo, G. Rocatello, F. Iannaccone, J. Degroote, J. Vierendeels, and P. Segers, “Fluid-structure interaction simulation of prosthetic aortic valves: Comparison between immersed boundary and arbitrary Lagrangian-Eulerian techniques for the mesh representation,” *PLoS One* **11**, e0154517 (2016).
- ⁵³T. E. Tezduyar and S. Sathe, “Modelling of fluid-structure interactions with the space-time finite elements: Solution techniques,” *Int. J. Numer. Methods Fluids* **54**, 855–900 (2007).
- ⁵⁴A. Khayyer, H. Gotoh, and Y. Shimizu, “On systematic development of FSI solvers in the context of particle methods,” *J. Hydrodyn.* **34**, 395–407 (2022).
- ⁵⁵C. Antoci, M. Gallati, and S. Sibilla, “Numerical simulation of fluid-structure interaction by SPH,” *Comput. Struct.* **85**, 879–890 (2007).
- ⁵⁶M. Liu and Z. Zhang, “Smoothed particle hydrodynamics (SPH) for modeling fluid-structure interactions,” *Sci. China: Phys., Mech. Astron.* **62**, 984701 (2019).
- ⁵⁷A. Zhang, P. Sun, F. Ming, and A. Colagrossi, “Smoothed particle hydrodynamics and its applications in fluid-structure interactions,” *J. Hydrodyn.* **29**, 187–216 (2017).

- ⁵⁸C. Zhang, Y. Zhu, D. Wu, N. A. Adams, and X. Hu, "Smoothed particle hydrodynamics: Methodology development and recent achievement," *J. Hydrodyn.* **34**, 767–805 (2022).
- ⁵⁹L. B. Lucy, "A numerical approach to the testing of the fission hypothesis," *Astron. J.* **82**, 1013 (1977).
- ⁶⁰R. A. Gingold and J. J. Monaghan, "Smoothed particle hydrodynamics: Theory and application to non-spherical stars," *Mon. Not. R. Astron. Soc.* **181**, 375–389 (1977).
- ⁶¹M. B. Liu and G. R. Liu, "Smoothed particle hydrodynamics (SPH): An overview and recent developments," *Arch. Comput. Methods Eng.* **17**, 25–76 (2010).
- ⁶²J. J. Monaghan, "Smoothed particle hydrodynamics and its diverse applications," *Annu. Rev. Fluid Mech.* **44**, 323–346 (2012).
- ⁶³G. Fourey, C. Hermange, D. L. Touzé, and G. Oger, "An efficient FSI coupling strategy between smoothed particle hydrodynamics and finite element methods," *Comput. Phys. Commun.* **217**, 66–81 (2017).
- ⁶⁴T. Long, D. Hu, D. Wan, C. Zhuang, and G. Yang, "An arbitrary boundary with ghost particles incorporated in coupled FEM–SPH model for FSI problems," *J. Comput. Phys.* **350**, 166–183 (2017).
- ⁶⁵S. L. Fuchs, C. Meier, W. A. Wall, and C. J. Cyron, "A novel smoothed particle hydrodynamics and finite element coupling scheme for fluid–structure interaction: The sliding boundary particle approach," *Comput. Methods Appl. Mech. Eng.* **383**, 113922 (2021).
- ⁶⁶S. M. Hosseini and J. J. Feng, "A particle-based model for the transport of erythrocytes in capillaries," *Chem. Eng. Sci.* **64**, 4488–4497 (2009).
- ⁶⁷X. Yang, M. Liu, S. Peng, and C. Huang, "Numerical modeling of dam-break flow impacting on flexible structures using an improved SPH–EBG method," *Coastal Eng.* **108**, 56–64 (2016).
- ⁶⁸G. Zhang, S. Wang, Z. Sui, L. Sun, Z. Zhang, and Z. Zong, "Coupling of SPH with smoothed point interpolation method for violent fluid–structure interaction problems," *Eng. Anal. Boundary Elem.* **103**, 1–10 (2019).
- ⁶⁹A. Monteleone, G. Borino, E. Napoli, and G. Burriesci, "Fluid–structure interaction approach with smoothed particle hydrodynamics and particle–spring systems," *Comput. Methods Appl. Mech. Eng.* **392**, 114728 (2022).
- ⁷⁰C. Zhang, M. Rezavand, and X. Hu, "A multi-resolution SPH method for fluid–structure interactions," *J. Comput. Phys.* **429**, 110028 (2021).
- ⁷¹A. Raffee and K. P. Thiagarajan, "An SPH projection method for simulating fluid–hypoelastic structure interaction," *Comput. Methods Appl. Mech. Eng.* **198**, 2785–2795 (2009).
- ⁷²A. Khayyer, H. Gotoh, H. Falahaty, and Y. Shimizu, "An enhanced ISPH–SPH coupled method for simulation of incompressible fluid–elastic structure interactions," *Comput. Phys. Commun.* **232**, 139–164 (2018).
- ⁷³A. Monteleone, S. Di Leonardo, E. Napoli, and G. Burriesci, "A novel mono-physics particle-based approach for the simulation of cardiovascular fluid–structure interaction problems," *Comput. Methods Programs Biomed.* **245**, 108034 (2024).
- ⁷⁴R. Gnyaneshwar, R. K. Kumar, and K. R. Balakrishnan, "Dynamic analysis of the aortic valve using a finite element model," *Ann. Thorac. Surg.* **73**, 1122–1129 (2002).
- ⁷⁵T. Ishihara, V. J. Ferrans, M. Jones, S. W. Boyce, O. Kawanami, and W. C. Roberts, "Histologic and ultrastructural features of normal human parietal pericardium," *Am. J. Cardiol.* **46**, 744–753 (1980).
- ⁷⁶F. Di Puccio, S. Celi, and P. Forte, "Review of experimental investigations on compressibility of arteries and introduction of a new apparatus," *Exp. Mech.* **52**, 895–902 (2012).
- ⁷⁷Y. C. Fung, *Biomechanics: Mechanical Properties of Living Tissues* (Springer Verlag, New York, NY, 1993).
- ⁷⁸A. Monteleone, A. Viola, E. Napoli, and G. Burriesci, "Modelling of thrombus formation using smoothed particle hydrodynamics method," *PLoS One* **18**, e0281424 (2023).
- ⁷⁹A. M. Lo Presti, A. Monteleone, G. Musotto, A. Tamburini, E. Napoli, and G. Burriesci, "Modelling of thrombus formation, growth and embolisation in the left atrial appendage under atrial fibrillation," *Comput. Biol. Med.* **191**, 110134 (2025).
- ⁸⁰A. Monteleone, M. Monteforte, and E. Napoli, "Inflow/outflow pressure boundary conditions for smoothed particle hydrodynamics simulations of incompressible flows," *Comput. Fluids* **159**, 9–22 (2017).
- ⁸¹J. Westerweel, G. E. Elsinga, and R. J. Adrian, "Particle image velocimetry for complex and turbulent flows," *Annu. Rev. Fluid Mech.* **45**, 409–436 (2013).
- ⁸²F. Kojo Chaway Acquah, J. Paul Konadu Takyi, and H. R. Beem, "Design and characterization of a low-cost particle image velocimetry system," *HardwareX* **19**, e00563 (2024).
- ⁸³M. D. Ford, H. N. Nikolov, J. S. Milner, S. P. Lownie, E. M. DeMont, W. Kalata, F. Loth, D. W. Holdsworth, and D. A. Steinman, "PIV-measured versus CFD-predicted flow dynamics in anatomically realistic cerebral aneurysm models," *J. Biomech. Eng.* **130**, 021015 (2008).
- ⁸⁴H. Yang, I. Hong, Y. B. Kim, K.-C. Cho, and J. H. Oh, "Influence of blood viscosity models and boundary conditions on the computation of hemodynamic parameters in cerebral aneurysms using computational fluid dynamics," *Acta Neurochir.* **165**, 471–482 (2023).
- ⁸⁵G. Annio, R. Torii, A. Ducci, V. Muthurangu, V. Tsang, and G. Burriesci, "Experimental validation of enhanced magnetic resonance imaging (EMRI) using particle image velocimetry (PIV)," *Ann. Biomed. Eng.* **49**, 3481 (2021).
- ⁸⁶E. Napoli, M. De Marchis, and E. Vitanza, "PANORMUS-SPH. A new smoothed particle hydrodynamics solver for incompressible flows," *Comput. Fluids* **106**, 185–195 (2015).
- ⁸⁷A. J. Chorin, "Numerical solution of the Navier–Stokes equations," *Math. Comput.* **22**, 745–762 (1968).
- ⁸⁸A. Monteleone, M. De Marchis, B. Milici, and E. Napoli, "A multi-domain approach for smoothed particle hydrodynamics simulations of highly complex flows," *Comput. Methods Appl. Mech. Eng.* **340**, 956–977 (2018).
- ⁸⁹H. A. van der Vorst, "Bi-CGSTAB: A fast and smoothly converging variant of Bi-CG for the solution of nonsymmetric linear systems," *SIAM J. Sci. Stat. Comput.* **13**, 631–644 (1992).
- ⁹⁰R. Xu, P. Stansby, and D. Laurence, "Accuracy and stability in incompressible SPH (ISPH) based on the projection method and a new approach," *J. Comput. Phys.* **228**, 6703–6725 (2009).
- ⁹¹J. W. Swegle, D. L. Hicks, and S. W. Attaway, "Smoothed particle hydrodynamics stability analysis," *J. Comput. Phys.* **116**, 123–134 (1995).
- ⁹²S. Liu, X. He, Y. Guo, Y. Chang, and W. Wang, "A dual-particle approach for incompressible SPH fluids," *ACM Trans. Graphics* **43**, 28 (2024).
- ⁹³R. Vacondio, C. Altomare, M. De Lefte, X. Hu, D. Le Touzé, S. Lind, J.-C. Marongiu, S. Marrone, B. D. Rogers, and A. Souto-Iglesias, "Grand challenges for smoothed particle hydrodynamics numerical schemes," *Comput. Part. Mech.* **8**, 575–588 (2021).
- ⁹⁴R. Budwig, "Refractive index matching methods for liquid flow investigations," *Exp. Fluids* **17**, 350–355 (1994).
- ⁹⁵S. F. Wright, I. Zadrazil, and C. N. Markides, "A review of solid–fluid selection options for optical-based measurements in single-phase liquid, two-phase liquid–liquid and multiphase solid–liquid flows," *Exp. Fluids* **58**, 108 (2017).
- ⁹⁶M. Raffel, C. E. Willert, F. Scarano, C. J. Kähler, S. T. Wereley, and J. Kompenhans, *Particle Image Velocimetry* (Springer International Publishing, Cham, 2018).
- ⁹⁷TSI, INSIGHT 4G, GLOBAL IMAGE, ACQUISITION, ANALYSIS, & DISPLAY SOFTWARE USER'S GUIDE (P/N 6004904, Revision E), TSI Incorporated, 2017.
- ⁹⁸J. J. Monaghan, "Smoothed particle hydrodynamics," *Annu. Rev. Astron. Astrophys.* **30**, 543–574 (1992).
- ⁹⁹L. He, X. Ban, X. Liu, and X. Wang, "Individual time stepping for SPH fluids," in *Eurographics (Short Papers)* (The Eurographics Association, 2015), pp. 41–44.
- ¹⁰⁰M. Ihmsen, N. Akinci, M. Gissler, and M. Teschner, "Boundary handling and adaptive time-stepping for PCISPH," in *Workshop on Virtual Reality Interaction and Physical Simulation VRIPHYS*, edited by J. Bender, K. Erleben, and M. Teschner (The Eurographics Association, 2010).
- ¹⁰¹A. Monteleone, G. Burriesci, and E. Napoli, "A distributed-memory MPI parallelization scheme for multi-domain incompressible SPH," *J. Parallel Distrib. Comput.* **170**, 53–67 (2022).
- ¹⁰²M. G. Olsen and R. J. Adrian, "Brownian motion and correlation in particle image velocimetry," *Opt. Laser Technol.* **32**, 621–627 (2000).
- ¹⁰³A. Sciacchitano, "Uncertainty quantification in particle image velocimetry," *Meas. Sci. Technol.* **30**, 092001 (2019).
- ¹⁰⁴J. J. Charonko and P. P. Vlachos, "Estimation of uncertainty bounds for individual particle image velocimetry measurements from cross-correlation peak ratio," *Meas. Sci. Technol.* **24**, 065301 (2013).

- ¹⁰⁵A. Masci, L. Barone, L. Dedè, M. Fedele, C. Tomasi, A. Quarteroni, and C. Corsi, “The impact of left atrium appendage morphology on stroke risk assessment in atrial fibrillation: A computational fluid dynamics study,” *Front. Physiol.* **9**, 1938 (2019).
- ¹⁰⁶D. Vella, A. Monteleone, G. Musotto, G. M. Bosi, and G. Burriesci, “Effect of the alterations in contractility and morphology produced by atrial fibrillation on the thrombosis potential of the left atrial appendage,” *Front. Bioeng. Biotechnol.* **9**, 586041 (2021).
- ¹⁰⁷L. Dedè, F. Menghini, and A. Quarteroni, “Computational fluid dynamics of blood flow in an idealized left human heart,” *Int. J. Numer. Method. Biomed. Eng.* **37**, e3287 (2021).
- ¹⁰⁸S. Turek and J. Hron, “Proposal for numerical benchmarking of fluid–structure interaction between an elastic object and laminar incompressible flow,” in *Fluid-Structure Interaction* (Springer, Berlin/Heidelberg, 2006), pp. 371–385.
- ¹⁰⁹S. Turek, J. Hron, M. Mádlík, M. Razzaq, H. Wobker, and J. F. Acker, “Numerical simulation and benchmarking of a monolithic multigrid solver for fluid-structure interaction problems with application to hemodynamics,” in *Fluid Structure Interaction II* (Springer, Berlin/Heidelberg, 2011), pp. 193–220.
- ¹¹⁰A. Goetz, P. J. Rico, Y. Chau, J. Sédat, A. Larcher, and E. Hachem, “Proposal for numerical benchmarking of fluid-structure interaction in cerebral aneurysms,” [arXiv:2308.08301](https://arxiv.org/abs/2308.08301) (2023).
- ¹¹¹R. Bhardwaj and R. Mittal, “Benchmarking a coupled immersed-boundary-finite-element solver for large-scale flow-induced deformation,” *AIAA J.* **50**, 1638–1642 (2012).
- ¹¹²G. Annio, R. Torii, B. Ariff, D. P. O’Regan, V. Muthurangu, A. Ducci, V. Tsang, and G. Burriesci, “Enhancing magnetic resonance imaging with computational fluid dynamics,” *J. Eng. Sci. Med. Diagn. Ther.* **2**, 041010 (2019).
- ¹¹³M. Bagheri, M. Mohammadi, and M. Riazzi, “A review of smoothed particle hydrodynamics,” *Comput. Part. Mech.* **11**, 1163–1219 (2024).